Materials Research. 2025; 28: e20250032
DOI: https://doi.org/10.1590/1980-5373-MR-2025-0032

Preparation and Comparison Between Bi_2WO_6 and ZnO Photoanodes in Dye-sensitized Solar Cells

Buagun Samran[a], Sumneang Lunput[b], Saranyoo Chaiwichian[b*]

[a]*Nakhon Phanom University, Faculty of Science, Mueang Nakhon Phanom, Nakhon Phanom, Thailand.*
[b]*Rajamangala University of Technology, Faculty of Industry and Technology, Department of Science and Mathematics, Phangkhon, Sakon Nakhon, Thailand.*

Received: January 07, 2025; Revised: May 08, 2025; Accepted: May 18, 2025

This study presents a comparative analysis of two photoanode materials such as bismuth tungstate (Bi_2WO_6) and zinc oxide (ZnO) for application in dye-sensitized solar cells (DSSCs). The Bi_2WO_6 and ZnO films were coated onto fluorine-doped tin oxide (FTO) glass substrate via the doctor blade method. The film samples were characterized by using XRD, SEM, TEM, XPS, FT-IR and UV-Vis-NIR techniques. The photovoltaic performance of DSSCs using MO and RhB dyes as sensitizers was assessed under solar light irradiation. Results revealed that Bi_2WO_6 and ZnO film photoanodes sensitized with MO dye showed superior photovoltaic efficiency compared to when sensitized with RhB dye. Moreover, the ZnO film photoanode achieved an efficiency of 1.24%, outperforming the Bi_2WO_6 film photoanode which had an efficiency of 0.85% under similar conditions. A probable mechanism for photogenerated electron transfer and charge carrier separation in DSSCs was proposed.

Keywords: *Bi_2WO_6, ZnO, Dye-sensitized solar cells.*

1. Introduction

Dye-sensitized solar cells (DSSCs) are sustainable and clean technologies for converting solar energy into electrical energy, first developed by O'Regan and Grätzel in 1991[1] and Grätzel in 2001[2]. DSSCs have gained great popularity due to their attractive features and advantages such as easy production process, low cost, high stability, and environmental friendly[3,4]. In general, DSSCs preparation is comprised of an oxide semiconductor film coated on a conductive glass substrate with sensitizing dyes as a photoanode, carbon powder or metal particles used as a counter electrode, and iodide/triiodide (I^-/I^{3-}) redox couple applied as an electrolyte in DSSCs[5]. In the past decade, the varieties of oxide semiconductors have been considered as photoanodes such as TiO_2, MgO, MnO_2, SnO_2, WO_3, ZnO and so on[6-11]. Among these oxide semiconductor materials, ZnO is one of the most significant oxide semiconductors, drawing wide attention of researchers for potential applications in DSSCs due to its high efficiency, lower cost, high physicochemical stabilities, small particle size, and wide band gap energy, which is similar to TiO_2[12,13]. Moreover, ZnO has a porous-like structure, leading to the adsorption of more dye molecules and the conduction of photoinduced electrons from dyes on the surface area[14,15], resulting in its enhanced photoconversion performance in DSSCs. Among all the proposed oxide semiconductors, the efficacy of Bi_2WO_6 particles in DSSCs has been reported. Bi_2WO_6 is one of the simplest Aurivillius oxide family with the general formula $Bi_2A_{n-1}B_nO_{3n+3}$ (A = Ca, Sr, Ba, Pb, Bi, Na, K and B = Ti, Nb, Ta, Mo, W, Fe), which has orthorhombic layered structure of the perovskite-like slaps of octahedral $(WO_4)^{2-}$ layers and alternating bismuth oxide $(Bi_2O_2)^{2+}$ layers[16-18]. To date, Bi_2WO_6 has gained great attention because it shows excellent properties for significant applications, including catalysts, optical fiber, ferroelectric piezoelectricity, pyroelectricity, magnetic devices, and so on[18]. Moreover, various methods have been employed to synthesize Bi_2WO_6 particles resulting in different structures such as hydrothermal, co-precipitation, sol-gel, microwave-assisted, solid-state reaction, flux growth, etc[19-24].

On the other hand, Bi_2WO_6 and ZnO films on the FTO glass substrate are used as photoanode materials in DSSCs. There are various methods such as screen-printing process[25], sol-gel process[26], physical vapor deposition process[27], electro-hydrodynamic deposition process[28], spin coating process[29], dip-coating process[30], and doctor blade process[31]. Especially, the doctor blade process is mainly mentioned as a preferable technique for preparing films owing to their easier production techniques and low cost. In addition, a film can be quickly prepared up to several meters per minute and the film thickness can be tuned from twenty nanometers to one hundred micrometers on the FTO glass substrate[32].

In this research, the doctor blade technique is used to produce Bi_2WO_6 and ZnO films on FTO glass substrate, as a photoanode for application in DSSCs. Moreover, the as-prepared films were coated with two synthetic dyes, MO and RhB for the use as sensitizers in DSSCs. Furthermore, the photovoltaic efficiency and mechanism of DSSCs were investigated by irradiating solar light.

*e-mail: saranyou530531117@gmail.com

2. Experimental Section

2.1. Preparation of Bi_2WO_6 particles

In a typical hydrothermal synthesis procedure, bismuth nitrate pentahydrate ($Bi(NO_3)_3$•$5H_2O$) and sodium tungstate dihydrate (Na_2WO_4•$2H_2O$) in a molar ratio of 2:1 were dissolved in 50 ml of diluted nitric acid (HNO_3) and deionized water, respectively. The solutions were mixed with a magnetic stirrer before adding ammonium hydroxide (NH_4OH) solution to adjust pH 7. Then, the as-prepared suspension was poured into 100 ml Teflon-lined stainless autoclave vessel and heated at 180 °C for 24 hours. After that, the suspension was washed with deionized water using a centrifuge to separate the precipitate and the solution, and then dried in an electric oven at 80 °C for 24 hours.

2.2. Preparation of ZnO particles

The ZnO particles were synthesized via a co-precipitation method. The zinc acetate dehydrate ($Zn(CH_3COO)_2 \cdot 2H_2O$) and potassium hydroxide (KOH) were used as starting materials. Firstly, $Zn(CH_3COO)_2 \cdot 2H_2O$ and KOH with 0.1:0.2 M ratio were dissolved in deionized water of 50 ml. The solutions were then mixed with vigorous magnetic stirring to form a homogeneous solution. The 6 M of nitric acid was diluted with deionized water to adjust the pH 7. The obtained precipitates were collected and filtered by a centrifuge and then dried with a muffled oven at 80 °C for 24 hours. Finally, the white ZnO particles were heated at 500 °C for 1 hour.

2.3. Preparation of DSSCs

First of all, the FTO glass substrate was cleaned with deionized water and ethanol in an ultrasonic bath to eliminate contaminants from the glass. Besides, the pastes were prepared by using 0.5 g of particle powders, 1 ml of acetic acid, 0.5 ml of Triton x-100, and 5 ml of absolute ethanol. Then the mixtures of the paste preparation were ground continuously in a mortar to form homogeneous pastes. The as-prepared pastes were coated on FTO glass substrate by the doctor blade method. Final films were annealed at a temperature of 450 °C for 1 hour to eliminate Triton x-100.

After that, the as-prepared films were soaked in dye solution for 24 hours to ensure absorption-desorption equilibrium for the use as a photocathode. For the part of the photoanode, the carbon powder decorated on FTO glass substrate was used. To estimate the photovoltaic efficiency, photocathode and photoanode were assembled to form a sandwich type.

2.4. Characterization

The phase structure of all film samples was recorded by X-ray diffraction (XRD, BRUKER, D8 Advance) using Cu Kα radiation, with the 2θ of samples ranging from 10° to 80°. The morphological characterization of as-prepared film samples was analyzed using scanning electron microscopy (SEM, HITACHI S-3400N). The actual microstructure of film samples was observed via transmission electron microscopy (TEM, JEOL model JEM 2100). The specific surface area of film samples was determined through Brunauer-Emmett-Teller (BET, 3 Flex Micromeritics). The chemical composition and surface electronic states of film samples were studied through X-ray photoelectron spectroscopy (XPS, AXIS ULTRA^{DLD}). The identification of functional groups of film samples was studied through Fourier transform infrared spectroscopy (FT-IR, PerkinElmer Scientific) technique. The optical absorption properties and band gap energies of film samples were measured via UV-VIS-NIR spectrophotometer (UV-vis, Shimadzu 3600).

3. Results and Discussion

3.1. XRD analysis

The crystallographic structure of Bi_2WO_6 and ZnO films was analyzed by using XRD technique. Figure 1 shows the XRD patterns of Bi_2WO_6 and ZnO films. The structure and phase purity of Bi_2WO_6 and ZnO films were confirmed. The XRD pattern of Bi_2WO_6 film typically indicated characteristic peaks that corresponded to the orthorhombic phase with a JCPDS file no. 73-1126[33]. The main diffraction peaks of Bi_2WO_6 film were observed at 2θ of approximately 28.31°, 32.87°, 47.13°, 55.91° and 58.56°. These peaks matched well with (113), (200), (220), (313) and (226) planes, respectively. For XRD pattern of ZnO film, the diffraction peaks were indexed as the hexagonal wurtzite crystal structure which related to a JCPDS file no. 36-1451[34]. The crucial diffraction peaks of ZnO film located at 31.79°, 34.44°, 36.27°, 47.54°, 56.57°, 62.87°, 67.93° and 69.09°. These intensities corresponded to (001), (002), (101), (102), (110), (103), (112) and (201) planes, respectively. Moreover, it can be seen that there was no other impurity phases, indicating that both orthorhombic Bi_2WO_6 and hexagonal wurtzite ZnO structures had high crystalline quality and purity.

3.2. SEM-TEM analysis

SEM technique was employed to investigate the morphology of ZnO and Bi_2WO_6 films, as shown in Figure 2. Figure 2a reveals the SEM image of ZnO film. The results demonstrated that the as-prepared ZnO film had a rod-like structure, with average particle size from ca. 20 to 50 nm. For SEM image of Bi_2WO_6 film, a plate-like structure with a large diameter of ca. 100 to 200 nm was found, as displayed in Figure 2b. To confirm the actual microstructure and particle size of ZnO and Bi_2WO_6 films, TEM technique

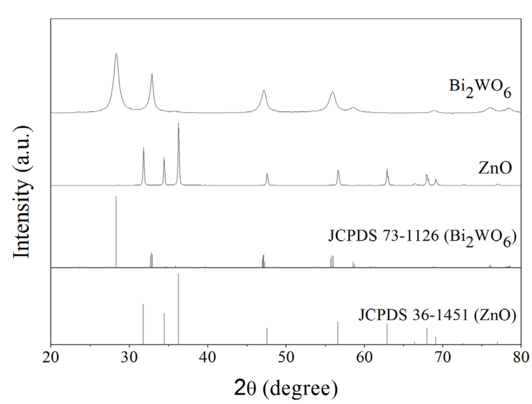

Figure 1. XRD patterns of Bi_2WO_6 and ZnO films.

was used. Figure 2c exhibits the microstructure of ZnO film. The structure was rod-like with ca. 50 to 100 nm in particle diameter. In part of Bi_2WO_6 film, a plate-like structure with a diameter ranging from ca. 100 to 200 nm was observed, as represented in Figure 2d.

3.3. XPS analysis

To study the information on the elemental composition of Bi_2WO_6 and ZnO film photoanodes, the X-ray photoelectron spectroscopy (XPS) technique was used and shown in Figure 3. It can be seen that the XPS spectrum of Bi_2WO_6 mainly composed of Bi 4f, W 4f and O 1s. As shown in Figure 3a, the intensity of Bi 4f was comprised of two peaks at 159.23 eV and 164.53 eV, which can be ascribed to Bi $4f_{7/2}$ and Bi $4f_{5/2}$ of Bi^{3+} ions in $[Bi_2O_2]^{2+}$ [35,36]. In Figure 3b, the peaks of W 4f located at a binding energy of 35.44 eV and 37.61 eV correspond to W $4f_{7/2}$ and W $4f_{5/2}$, respectively, which can be attributed to W^{6+} ions in $[WO_4]^{2-}$ [35,36]. The O 1s peaks of Bi_2WO_6 had four binding energies which appeared at 530.16 eV, 531.35 eV, 532.95 eV, and 534.32 eV, matching Bi-O (lattice oxygen), W-O, OH groups, and oxygen species on the Bi_2WO_6 surface[37-39], respectively, as displayed in Figure 3c. For XPS spectrum of ZnO, it constituted the chemical states of Zn 2p and O 1s. In Figure 3d, it shows the XPS peaks of Zn 2p, which included two peaks at binding energy of 1021.68 eV for Zn $2p_{3/2}$ and 1044.70 eV for Zn $2p_{1/2}$, which can be assigned to Zn^{2+} ions in the form of ZnO[40,41]. The XPS peaks of O 1s displayed in Figure 3e can consist of four binding energies at 530.49 eV, 531.53 eV, 532.44 eV, and 533.65 eV, which identified chemisorbed O_2 species, OH groups in wurtzite hexagonal ZnO structure and lattice oxygen species in chemisorbed H_2O, respectively[40,41]. Therefore, the results of XPS analysis can be concluded that the existences of Bi, W, and O elements in Bi_2WO_6 and Zn, O elements in ZnO, correspond to the results of XRD analysis. film.

3.4. FT-IR analysis

Figure 4 displays the FT-IR spectra of Bi_2WO_6 and ZnO films, which were measured in the wavenumber region of 400-4000 cm^{-1} through the KBr method. From the FT-IR analysis results, the absorption bands of Bi_2WO_6 film appeared at 572 cm^{-1} could be attributed to the asymmetric stretch of Bi-O-Bi[42,43], while the peaks at 729 cm^{-1} and 1030 cm^{-1} were stretching of W-O, and the peak at 876 cm^{-1} was stretching mode of Bi-O[42,43]. The two absorption bands located at

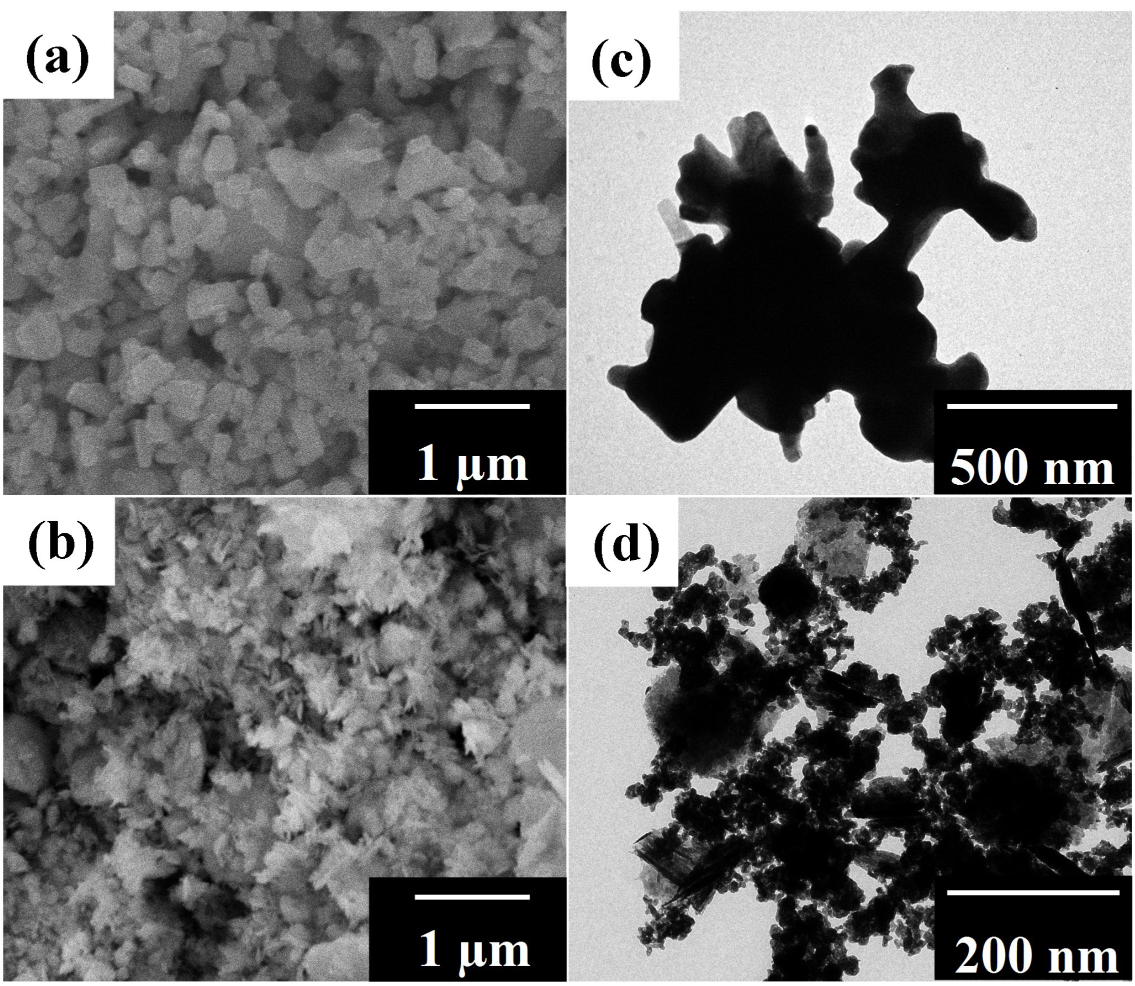

Figure 2. SEM and TEM images of (a,c) ZnO and (b,d) Bi_2WO_6 films.

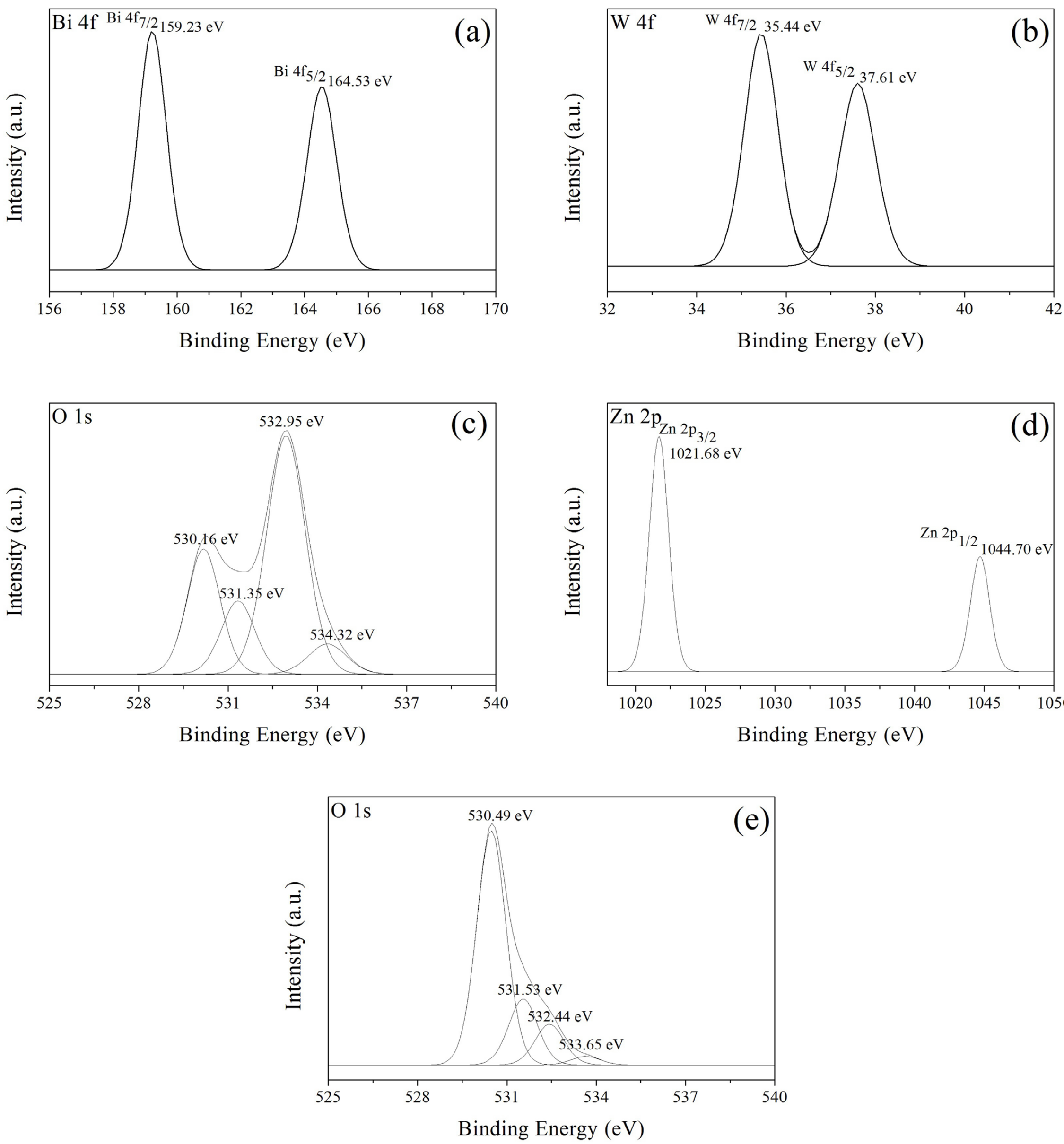

Figure 3. XPS spectra of (a) Bi 4f, (b) W 4f and (c) O 1s in Bi_2WO_6 film and (d) Zn 2p and O 1s in ZnO film.

1618 cm^{-1} and 3425 cm^{-1} could be matched well with the stretching and bending modes of O-H on the surface of Bi_2WO_6[44]. For the FT-IR peaks of ZnO film, the band of functional groups was showed at the wavenumber range of 832 cm-[1], 983 cm^{-1}, 1386 cm^{-1}, and 1519 cm^{-1}, corresponding to the bending vibration of C-H, stretching of C-N, bending vibration of C-H of an alkane group and stretching of C=C of an aromatic ring[45,46], respectively. The peaks at 2363 cm^{-1} and 3405 cm^{-1} corresponded to the vibration of H-O-H of water molecules and the stretching vibration of O-H of hydroxyl compounds[46,47], respectively.

3.5. UV-VIS-NIR analysis

The optical absorption and energy band structure of Bi_2WO_6 and ZnO films were carried out by using UV-vis NIR spectroscopy technique, as shown in Figure 5. The absorbance of Bi_2WO_6 and ZnO films can be calculated by using transmittance and reflectance measurements according to the equation as follows[48]:

$$\%A = 100 - (\%R - \%T) \tag{1}$$

where A is the absorbance, R is the reflectance and T is the transmittance, respectively. From experimental results, the absorption edges of Bi_2WO_6 and ZnO films showed the UV light range of ca 363 nm and 382 nm, respectively, as displayed in Figure 5a and 5b. The band gap energy of Bi_2WO_6 and ZnO films can be expressed via Tauc's formula as follows:

$$(\alpha h\nu) = A(h\nu - E_g)^n \tag{2}$$

where α is the absorption coefficient, *h* is the Planck's constant, *A* is the constant, *v* is the frequency of photons, E_g is the band gap energy of film samples and *n* is the type of optical transition of film samples: $n = \frac{1}{2}$ for direct optical transition and *n* = *2* for an indirect optical transition[49-51]. The band gap values of Bi_2WO_6 and ZnO films were plotted between $(\alpha hv)^N$ versus *hv* of the film samples, as represented in Figure 5c and 5d. The band gap energies of Bi_2WO_6 and ZnO films were found to be 3.39 eV and 3.24 eV, respectively. The absorption edge and band gap energy are key factors that affect the improved efficiency of DSSCs.

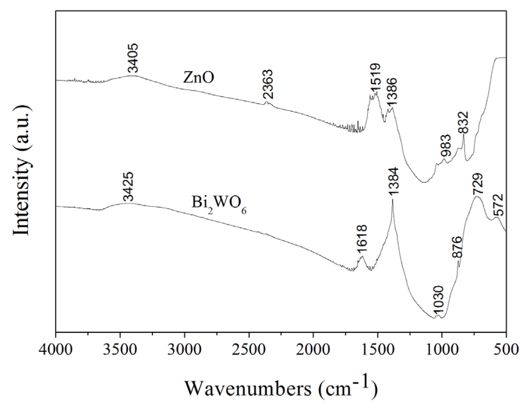

Figure 4. FT-IR spectrum of Bi_2WO_6 and ZnO film photoanodes.

3.6. Photoabsorption properties of synthetic dyes

Figure 6 shows the photoabsorption analysis of synthetic dyes such as methyl orange (MO) and rhodamine B (RhB), in which UV-vis spectrophotometer technique was employed. For the photoabsorption of MO and RhB dyes, maximum intensities appeared at 466 nm and 553 nm, respectively. Furthermore, the UV-vis spectra of MO dye located at 350-550 nm, which was in the wavelength range of UV and visible light. For the absorbance of RhB dye, it was in the visible light region of ca. 450-600 nm. The obtained results of photoabsorption in Figure 6 affected the π-π* transition of electrons on the dye surface. Moreover, it was found that MO dye showed a broader absorption region compared to RhB dye, indicating that MO dye showed the highest π-π* transition of electrons from LUMO of dye to conduction band of Bi_2WO_6 and ZnO film photoanodes as compared to RhB dye[52,53]. Therefore, it can be concluded that using MO dye as a sensitizer on the surface of Bi_2WO_6 and ZnO film photoanodes is more suitable than RhB dyes for potential application in DSSCs.

3.7. Photovoltaic efficiency of Bi_2WO_6 and ZnO film photoanodes

The photovoltaic efficiency was investigated by using Bi_2WO_6 and ZnO film photoanodes coated with two synthetic dyes as photoelectrodes in DSSCs. Figure 7 shows the plot of current density (J_{SC}) versus open-circuit voltage (V_{OC}). All parameters of photovoltaic efficiency study of Bi_2WO_6 and

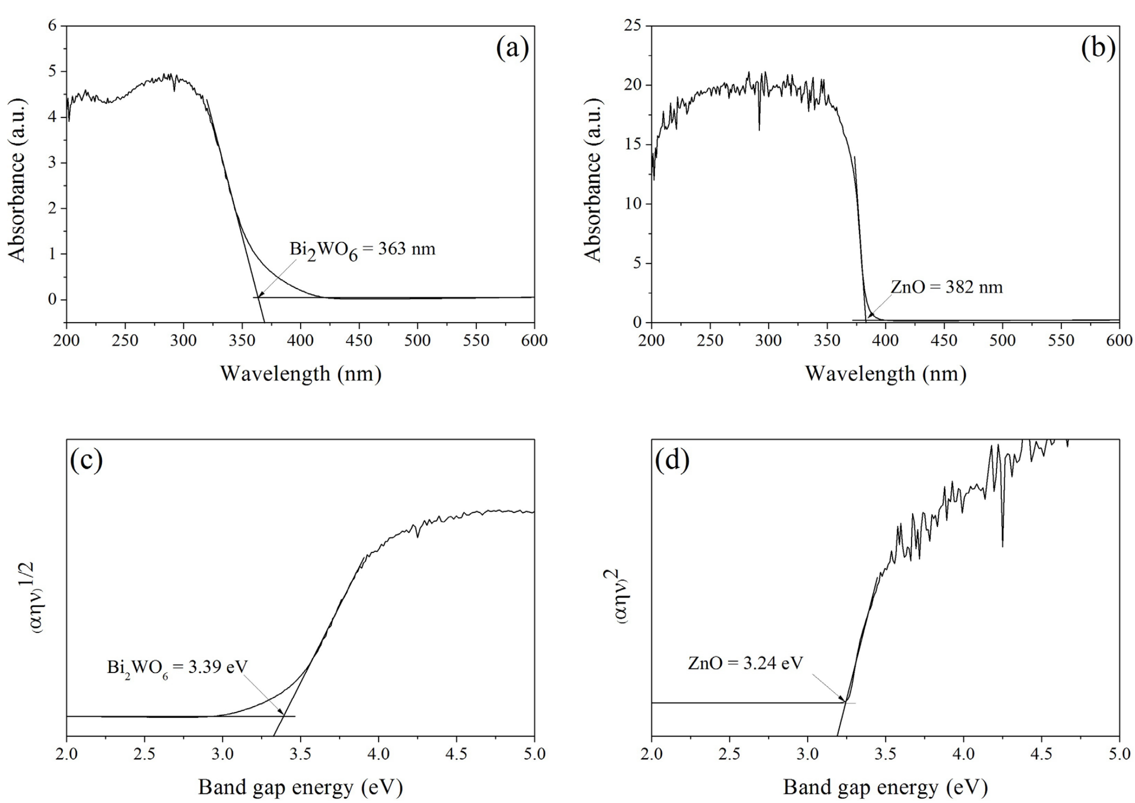

Figure 5. Optical absorption and band gap energy of (a,c) Bi_2WO_6 and (b,d) ZnO film photoanodes.

ZnO film photoanodes in DSSCs are shown in Tables 1 and 2. In addition, the solar cell conversion efficiency (η) of DSSCs based on Bi_2WO_6 and ZnO film photoanodes with synthetic dyes can be calculated from the following equation[54-56]:

$$FF = P_{max} / J_{SC} x V_{OC} \quad (3)$$

$$\eta(\%) = J_{SC} x V_{OC} x FF x \, 100 / P_{in} \quad (4)$$

where P_{max} is the ratio of the maximum power of solar cells per unit area divided by the J_{SC} and V_{OC}, J_{SC} is the short circuit current, V_{OC} is the open-circuit voltage, FF is the fill factor and P_{in} is the input power (100 mW/cm²). The results of Bi_2WO_6 film photoanode-based DSSCs with MO and RhB dyes showed 0.85% (J_{SC} is 6.103 mA/cm², V_{OC} is 0.500 V and FF is 0.28) and 0.45% (J_{SC} is 4.054 mA/cm², V_{OC} is 0.533 V and FF is 0.21), respectively, as shown in Figure 7a and Table 1. In the part of ZnO film photoanode-based DSSCs with MO and RhB dyes, the photovoltaic efficiency was equal to 1.24% (J_{SC} is 9.56 mA/cm², V_{OC} is 0.450 V and FF is 0.29) and 0.98% (J_{SC} is 8.1 mA/cm², V_{OC} is 0.450 V and FF is 0.27), respectively, as displayed in Figure 7b and Table 2. From the experimental results, it was found that using MO dye as the sensitizer in DSSCs showed the highest efficiency as compared to other dyes. This phenomenon may be due to MO dye having a broader photoabsorption in UV and visible light region than that of RhB dye[57-60], as represented in Figure 8. For the efficiency comparison study between Bi_2WO_6 and ZnO film photoanodes in DSSCs, it was found that ZnO film photoanode-based DSSCs exhibited higher efficiency than Bi_2WO_6 film photoanode-based DSSCs, which might be attributed to the transformation of electron from dye molecules to conduction band of ZnO film photoanode-based DSSCs, which was higher than Bi_2WO_6 film photoanode-based DSSCs[61]. Moreover, enhanced photovoltaic efficiency does not only depend on photoabsorption region and transformation of electrons, but also on crystal structure, specific surface area, microstructure, and so on[58].

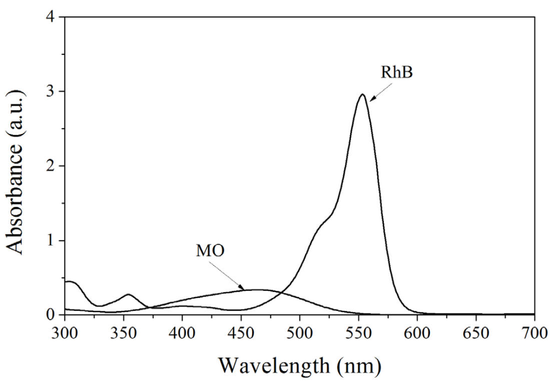

Figure 6. Photoabsorption spectra of synthetic dyes.

3.8. A possible mechanism of DSSCs

A possible mechanism of Bi_2WO_6 and ZnO film photoanodes-based DSSCs was studied and shown in Figure 9. The values

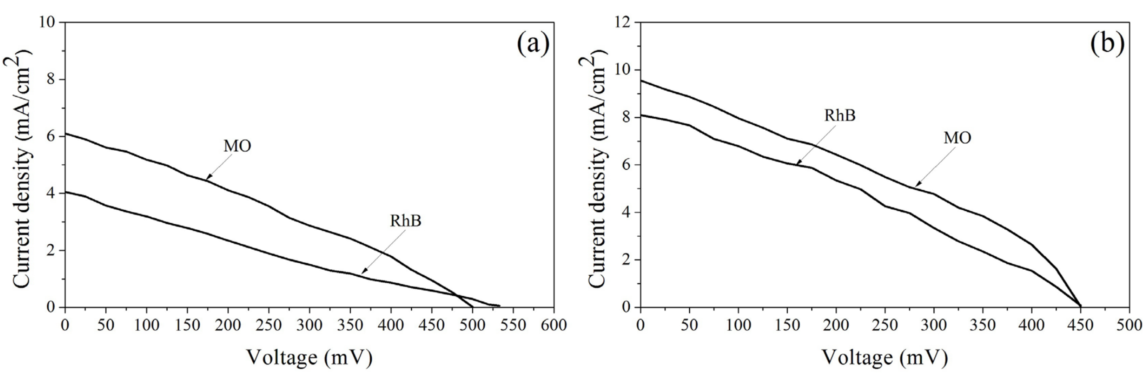

Figure 7. J-V curves of DSSCs using (a) Bi_2WO_6 and (b) ZnO film photoanodes with two synthetic dyes.

Table 1. Photovoltaic parameters of Bi_2WO_6 film photoanode-based DSSCs with synthetic dyes.

Synthetic dyes	J_{SC} (mA/cm²)	V_{OC} (V)	FF	η (%)
Methyl orange (MO)	6.103	0.500	0.28	0.85
Rhodamine B (RhB)	4.054	0.533	0.21	0.45

Table 2. Photovoltaic parameters of DSSCs based on ZnO photoanode with synthetic dyes.

Synthetic dyes	J_{SC} (mA/cm²)	V_{OC} (V)	FF	η (%)
Methyl orange (MO)	9.56	0.450	0.29	1.24
Rhodamine B (RhB)	8.10	0.450	0.27	0.98

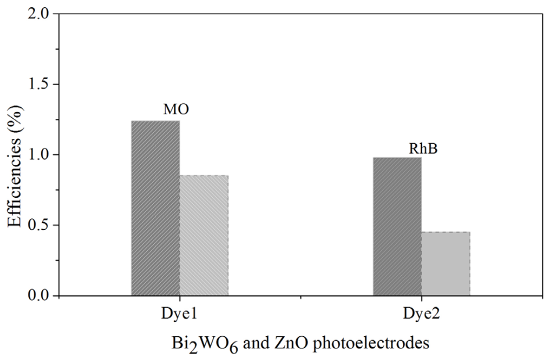

Figure 8. Comparison of photovoltaic efficiencies.

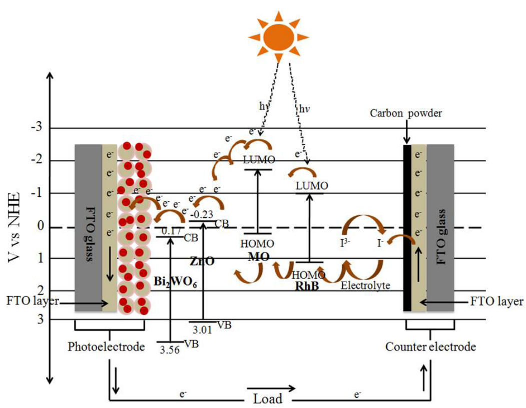

Figure 9. Schematic diagram of a possible mechanism of DSSCs.

of the conduction band (CB) and valence band (VB) offsets can be estimated by using the equation as follows[62]:

$$E_{CB} = \chi - E^C - 0.5E_g \tag{5}$$

$$E_{VB} = E_{CB} + E_g \tag{6}$$

where E_{CB} is the energy level of the conduction band edge of a semiconductor, E_{VB} is the energy level of the valence band edge of the semiconductor, χ is the absolute electronegativity of the semiconductor (χ is 5.89 eV for ZnO[63], χ is 6.36 eV for Bi_2WO_6[64]), E^C is the energy of free electrons on the hydrogen scale (~4.5) and E_g is the band gap energy of the semiconductor. The values of CB and VB edges of Bi_2WO_6 derived from equations 3 and 4 were 0.17 eV and 3.56 eV, and of ZnO were -0.23 eV and 3.01 eV, respectively. The basic compositions of DSSCs are mainly composed of FTO glass substrate, semiconductor oxide photoanodes, dyes, electrolytes, and counter electrodes. A likely mechanism of DSSCs was illuminated by solar light. The synthetic dye sensitizer has higher absorbance than photon energy or equal to the band gap energy of the dye sensitizer to excite the photogenerated electron transfer from HOMO to LUMO level of the dye sensitizer and finally become photoexcited. The separation of photogenerated charge carriers occurred in the dye sensitizer and interface of semiconductor oxide photoanodes when the electrons and holes are located at the semiconductor oxide photoanodes and oxidized dye sensitizer. The electrons on LUMO of the dye sensitizer are injected into the CB of semiconductor oxide photoanodes, which is lower in energy than the excited state of the dye sensitizer. Then the photogenerated electrons flow into the photoelectrode to transfer positive charges to the counter electrode, which is connected to the working electrode through the external load. Furthermore, electrons from the dye sensitizer can be injected from iodine electrolyte through iodide (I^-)ions to become triiodide (I^{3-})ions, releasing photogenerated charges. Finally, the photogenerated charges flow from the external load and reverse to DSSCs via the carbon counter electrode on FTO glass substrate[65,66]. This process is repeated to generate electric power by irradiating solar light.

4. Conclusions

In summary, two synthetic dyes, MO and RhB were employed as the sensitizers for DSSCs. The Bi_2WO_6 and ZnO films decorated on FTO glass substrate as photoanodes were prepared through the doctor blade method. A comparison of photovoltaic efficiency of film photoanodes and two synthetic dyes under similar conditions was investigated. The result indicated that coating MO dye on film photoanodes in DSSCs gave better efficiency than RhB dye owing to its broader photoabsorption region. Moreover, it was found that ZnO film photoanode showed better photovoltaic efficiency than Bi_2WO_6 film photoanode. As a result, it can be concluded that the ZnO film photoanode as a photoelectrode and MO dye as a sensitizer are suitable for application in DSSCs due to better bonding of dye molecules to ZnO film photoanode and better transitions of electrons from LUMO of dye molecules to conduction band edge of ZnO film photoanode. Therefore, to maximize the potential for improving the efficiency of DSSCs in the future, we may be considered the modifying Bi_2WO_6 through doping, morphology control, or hybrid designs.

5. Acknowledgements

The authors are appreciative to the Department of Science and Mathematics, Faculty of Industry and Technology, Rajamangala University of Technology Isan Sakonnakhon Campus, and the Division of Physics, Faculty of Science, Nakhon Phanom University for supporting this research.

6. References

1. O'Regan B, Grätzel M. A low-cost, high-efficiency solar cell based on dye sensitized colloidal TiO_2 films. Nature. 1991;353:737-40.
2. Grätzel M. Photelectrochemical cells. Nature. 2001;414:338-44.
3. Rajaei E, Ravandi SAH, Valipouri A. Electrochemical and photovoltaic properties of dye-sensitized solar cells based on Ag-doped TiO_2 nanorods. Optik (Stuttg). 2018;158:514-21.
4. Iqbal Z, Wu WQ, Zang H. Impact of hydroxy and octyloxy substituents of phenothiazine based dyes on the photovoltaic performance Dyes. Pigm. 2013;99:299-307.
5. Yalcin M, Yakuphanoglu F. Voltage and frequency dependence of negative capacitance behavior in a Graphene-TiO_2 nanocomposite photoanode based on quantum dot sensitized solar cells. Optik (Stuttg). 2019;83:1099-105.
6. Gnida P, Jarka P, Chulkin P, Schab-Balcerzak E. Impact of TiO_2 nanostructures on dye-sensitized solar cells performance. Mater. 2021;14:1633.

7. Merazga A, Al-Subai F, Albaradi AM. Effect of sol–gel MgO spin-coating on the performance of TiO_2-based dye-sensitized solar cells. Mater Sci Semicond Process. 2016;41:114-20.
8. Ahmada K, Mohammada A, Mobina SM. Hydrothermally grown a-MnO_2 nanorods as highly efficient low cost counter-electrode material for dye-sensitized solar cells and electrochemical sensing applications. Electrochim Acta. 2017;252:549-57.
9. Zainudin SNF, Abdullah H, Markom M. Electrochemical studies of tin oxide based-dye-sensitized solar cells (DSSC): a review. J Mater Sci Mater Electron. 2019;30:5342-56.
10. Zheng H, Tachibana Y, Kalantar-zadeh K. Dye-sensitized solar cells based on WO_3. Langmuir. 2010;26(24):19148-52.
11. Ossai AN, Alabi AB, Ezike SC. Zinc oxide-based dye-sensitized solar cells using natural and synthetic sensitizers. Curr Res Green Sustain Chem. 2020;3:100043.
12. Gonzalez-Valls I, Lira-Cantu M. Vertically-aligned nanostructures of ZnO for excitonic solar cells: a review. Energy Environ Sci. 2009;2(1):19-34.
13. Kannan S, Subiramaniyam NP, Lavanisadevi SU. Dye-sensitized solar cells based on TiO_2 nanoparticlesdecorated ZnO nanorod arrays for enhanced photovoltaic performance. J Mater Sci Mater Electron. 2020;31(7):3705-14.
14. Ko SH, Lee D, Kang HW. Nanoforest of hydrothermally grown hierarchical ZnO nanowires for a high efficiency dye-sensitized solar cell. Nano Lett. 2011;11:666-71.
15. Vittal R, Ho KC. Zinc oxide based dye-sensitized solar cells: a review. Renew Sustain Energy Rev. 2017;70:920-35.
16. Wang J, Li J, Zhao N. {010}-Oriented micro-flower-like hierarchical Bi_2WO_6 with high adsorptivity and visible-light-driven photoactivity: experimental studies and first-principles modeling. Appl Surf Sci. 2015;324:698-704.
17. Ge M, Li Y, Liu L. Bi_2O_3-Bi_2WO_6 composite microspheres: hydrothermal synthesis and photocatalytic performances. J Phys Chem C. 2011;115:5220-5.
18. Zhang L, Wang H, Chen Z. Bi_2WO_6 micro/nano-structures: synthesis, modifications and visible-light-driven photocatalytic applications. Appl Catal B. 2011;106:1-13.
19. Nagyné-Kovács T, Shahnazarova G, Lukács IE. Effect of pH in the hydrothermal preparation of Bi_2WO_6 nanostructures. Mater. 2019;12:1728.
20. Aouni AE, Ouardi ME, Arab M. Design of Bismuth Tungstate Bi_2WO_6 Photocatalyst for Enhanced and Environmentally Friendly Organic Pollutant Degradation. Mater. 2024;17:1029.
21. Han TY, Wang X, Ma YC. Mesoporous Bi_2WO_6 sheets synthesized via a sol–gel freeze-drying method with excellent photocatalytic performance. J Sol-Gel Sci Technol. 2017;82:101-8.
22. Liu XC, Wang SZ, Wang S. The three-dimensional flower-like Bi_2WO_6 assisted by ethanolamine through a microwave method for efficient photocatalytic activity. R Soc Open Sci. 2019;6:181422.
23. Zhang C, Zhu YF. Synthesis of Square Bi_2WO_6 Nanoplates as High-Activity Visible-Light-Driven Photocatalysts. Chem Mater. 2005;17:3537-45.
24. Li CM, Chen G, Sun JX. A novel mesoporous single-crystal-like Bi_2WO_6 with enhanced photocatalytic activity for pollutants degradation and oxygen production. ACS Appl Mater Interfaces. 2015;7:25716-24.
25. Huang AN, Pien WC, Kuo HP. Preparation of the working electrode of dye-sensitized solar cells using screen printing with alkyd resins. Energy Procedia. 2014;61:1528-31.
26. Cho TY, Ko KW, Yoon SG. Efficiency enhancement of flexible dye-sensitized solar cell with solegel formed Nb_2O_5 blocking layer. Curr Appl Phys. 2013;13(7):1391-6.
27. Negrea D, Ducu C, Moga S. Solar physical vapor deposition preparation and microstructural characterization of TiO_2 Based nanophases for dye-sensitized solar cell application. J Nanosci Nanotechnol. 2012;12:1-5.
28. Zhang ZF, He HJ, Fu WL. Electro-hydrodynamic direct-writing technology toward patterned ultra-thin fibers: advances, materials and applications. Nano Today. 2020;35:100942.
29. Sadikin SN, Rahman MYA, Umar AA. Effect of spin-coating cycle on the properties of TiO_2 thin film and performance of DSSC. Int J Electrochem Sci. 2017;12:5529-38.
30. Ahmadi S, Asim N, Alghoul MA. The role of physical techniques on the preparation of photoanodes for dye sensitized solar cells. Int J Photoenergy. 2014;19:198734.
31. Gomesh N, Ibrahim AH, Syafinar R. Fabrication Of Dye Sensitized Solar Cell Using Various Counter Electrode Thickness. Int J Eng Sci. 2015;1(1):49-56.
32. Ruani G, Ancora C, Corticelli F, Dionigi C, Rossi C. 2008 Single-step preparation of inverse opal titania flms by the doctor blade technique. Sol Energy Mater Sol Cells. 2008;92:537-42.
33. Ait Ahsaine H. El jaouhari A, Slassi A. Electronic band structure and visible-light photocatalytic activity of Bi_2WO_6: elucidating the effect of lutetium doping. RSC Advances. 2016;6:101105-14.
34. Basnet P, Samanta D, Chanu TI. Assessment of synthesis approaches for tuning the photocatalytic property of ZnO nanoparticles. SN Appl Sci. 2019;1:633.
35. Huang X, Li M, Guo Y. Hollow nest-like Bi/Bi_2WO_6 photocatalyst with coupled active effects of SPR and defective oxygen. J Mater Sci Mater Electron. 2022;33:19447-61.
36. Tian J, Sang Y, Yu GA. Bi_2WO_6-based hybrid photocatalyst with broad spectrum photocatalytic properties under UV, visible, and near-infrared irradiation. Adv Mater. 2013;25:5075.
37. Wang Q, Wu H, Wang Y. Ex-situ XPS analysis of yolk-shell Sb_2O_3/WO_3 for ultra-fast acetone resistive sensor. J Hazard Mater. 2021;412:125175.
38. Sun M, Zhang W, Sun Y. Synergistic integration of metallic Bi and defects on BiOI: enhanced photocatalytic NO removal and conversion pathway. Chin J Catal. 2019;40:826.
39. Gao Y, Shan X, Yang W. Structure regulation and photocatalytic activity enhancement of Bi_2WO_6 by "double-effect modification" mode. Int J Energy Res. 2019;43(13):7364.
40. Qu G, Fan G, Zhou M. Graphene-Modified ZnO Nanostructures for Low-Temperature NO_2 Sensing. ACS Omega. 2019;4:4221-32.
41. Claros M, Setka M, Jimenez YP. AACVD Synthesis and Characterization of Iron and Copper Oxides Modified ZnO Structured Films. Nanomater. 2020;10:471.
42. Chen F, Li D, Luo BF. Two-dimensional heterojunction photocatalysts constructed by graphite-like C_3N_4 and Bi_2WO_6 nanosheets: enhanced photocatalytic activities for water purification. J Alloys Compd. 2017;694:193-200.
43. Yu JG, Xiong JF, Cheng B. Hydrothermal preparation and visible-light photocatalytic activity of Bi_2WO_6 powders. J Solid State Chem. 2005;178:1968-72.
44. Zhao YY, Wang YB, Liu EZ. Bi_2WO_6 nanoflowers: an efficient visible light photocatalytic activity for ceftriaxone sodium degradation. Appl Surf Sci. 2018;436:854-64.
45. Santhoshkumar J, Kumar SV, Rajeshkumar S. Synthesis of zinc oxide nanoparticles using plant leaf extract against urinary tract infection pathogen. Resour Effic Technol. 2017;3:459-65.
46. Mahalakshmi S, Hema N, Vijaya PP. In vitro biocompatibility and antimicrobial activities of zinc oxide nanoparticles (zno nps) prepared by chemical and green synthetic route- a comparative study. BioNanoSci. 2020;10:112-21.
47. Muhammad W, Ullah N, Haroon M. Optical, morphological and biological analysis of zinc oxide nanoparticles (ZnO NPs) using Papaver somniferum L. RSC Advances. 2019;9:29541-8.
48. Sayama K, Nomura A, Arai T. Photoelectrochemical decomposition of water into H_2 and O_2 on porous $BiVO_4$ thin-film electrodes under visible light and significant effect of Ag ion treatment. J Phys Chem B. 2006;110:11352-60.

49. Zhou B, Qu J, Zhao X. Fabrication and photoelectrocatalytic properties of nanocrystalline monoclinic $BiVO_4$ thin-film electrode. J Environ Sci (China). 2011;23(1):151-9.
50. Huang C, Chen LL, Li HP. Synthesis and application of Bi_2WO_6 for the photocatalytic degradation of two typical fluoroquinolones under visible light irradiation. RSC Advances. 2019;9:27768-79.
51. Salari H, Kohantorabi M. Fabrication of novel Fe_2O_3/MoO_3/AgBr nanocomposites with enhanced photocatalytic activity under visible light irradiation for organic pollutant degradation. Adv Powder Technol. 2020;31:493-503.
52. Huang ZS, Cai C, Zang XF. Effect of the linkage location in the double branched organic dyes on the photovoltaic performance of the DSSCs. J Mater Chem A Mater Energy Sustain. 2015;3:1333-44.
53. Fan J, Liu S, Yu J. Enhanced photovoltaic performance of dye-sensitized solar cells based on TiO_2 nanosheets/graphene composite flms. J Mater Chem. 2012;22(33):17027-36.
54. Saravanan S, Kato R, Balamurugan M. Efficiency improvement in dye sensitized solar cells by the plasmonic effect of green synthesized silver nanoparticles. J Sci Adv Mater. 2017;2:418-24.
55. Li B, Wang L, Kang B. Review of recent progress in solid-state dye-sensitized solar cells. Sol Energy Mater Sol Cells. 2006;90:549-73.
56. Kong FT, Dai SY, Wang KJ. Review of recent progress in dyesensitized solar cells. Adv Opt Technol. 2006;1–2.
57. Pervez A, Javed K, Iqbal Z. Fabrication and comparison of dye-sensitized solar cells by using TiO_2 and ZnO as photo electrode. Optik (Stuttg). 2019;182:175-80.
58. Amornpitoksuk P, Suwanboon S, Randorn C. Photocatalytic activities of silver compound modified activated carbon@ ZnO: novel ternary composite visible light-driven photocatalysts. Mater Sci Semicond Process. 2018;84:50-5.
59. Alardhi SM, Fiyadh SS, Salman AD, Adelikhah M. Prediction of methyl orange dye (MO) adsorption using activated carbon with an artifcial neural network optimization modeling. Heliyon. 2023;9:e12888.
60. Dutta RK, Bhat SN. Interaction of methyl orange with submicellar cationic surfactants. Bull Chem Soc Jpn. 1993;66:2457-60.
61. Quintana M, Edvinsson T, Hagfeldt A. Comparison of dye-sensitized ZnO and TiO_2 solar cells: studies of charge transport and carrier life time. J Phys Chem C. 2007;111:1035-41.
62. Xu Y, Schoonen MAA. The absolute energy positions of conduction and valence bands of selected semiconducting minerals. Am Mineral. 2000;85:543-56.
63. Tatykayev B, Donat F, Alem H. Synthesis of core/shell ZnO/rGO nanoparticles by calcination of ZIF8/rGO composites and their photocatalytic activity. ACS Omega. 2017;2:4946-54.
64. Zhang ZJ, Wang WZ, Wang L. Enhancement of visible-light photocatalysis by coupling with narrow-band-gap semiconductor: a case study on Bi_2S_3/Bi_2WO_6. ACS Appl Mater Interfaces. 2012;4:593-7.
65. Rani M, Tripathi SK. A comparative study of nanostructured TiO_2, ZnO and bilayer TiO_2/ZnO dye-sensitized solar cells. J Electron Mater. 2015;44(4):1151-9.
66. Meng S, Ren J, Kaxiras E. Natural dyes adsorbed on TiO_2 nanowire for photovoltaic applicaitons: enhanced light absorption and ultrafast electron injection. Nano Lett. 2008;8:3266-72.

Data Availability

The data that support the findings of this study are available from the corresponding author upon reasonable request.